PCCP

Deconvolving lithium-ion redox in vanadium-iron oxide aerogels using X-ray absorption spectroscopy and density functional theory

Journal:	*Physical Chemistry Chemical Physics*
Manuscript ID	CP-ART-11-2024-004351.R2
Article Type:	Paper
Date Submitted by the Author:	25-Feb-2025

Complete List of Authors:	DeBlock, Ryan; US Naval Research Laboratory, Surface Chemistry Branch Johannes, Michelle; US Naval Research Laboratory, Center for Materials Physics and Technology Ford, Hunter; US Naval Research Laboratory, Surface Chemistry Branch Swift, Michael; US Naval Research Laboratory, Center for Materials Physics and Technology Rolison, Debra; US Naval Research Laboratory, Surface Chemistry Branch Long, Jeffrey; US Naval Research Laboratory, Surface Chemistry Branch

ARTICLE

Deconvolving lithium-ion redox in vanadium-iron oxide aerogels using X-ray absorption spectroscopy and density functional theory

Received 00th January 20xx,
Accepted 00th January 20xx

DOI: 10.1039/x0xx00000x

Ryan H. DeBlock,[a] Michelle D. Johannes,[b] Hunter O. Ford,[a] Michael W. Swift,[b] Debra R. Rolison[a] and Jeffrey W. Long *[a]

Substitution of vanadium into earth-abundant maghemite iron oxide introduces cation vacancies that increase Li^+ storage capacity concomitant with a positive shift in its electrochemical potential. Expressing vanadium ferrite (VFe_2Ox) as an aerogel offers an opportunity to probe Li^+ storage in this inherently defective spinel from highly disordered (X-ray amorphous) to nanocrystalline. To understand the redox sequence of the host cations, we use *in situ* X-ray absorption near-edge spectroscopy (XANES) obtained using an in-lab X-ray absorption spectrometer in concert with density functional theory calculations to uncover the quantum mechanical-level effects that underpin relevant energy-storage behaviors. The Fe K-edge spectra indicate that upon Li^+ insertion, the change in Fe oxidation state occurs primarily at high voltage (average voltage ~2.9 V), which is ~0.7 V higher than the average voltage for γ-Fe_2O_3. Parallel computations using density functional theory show that tetrahedral V and octahedral Fe sites are reduced during lithiation and that the hybridization of Fe and V orbitals imposes a positive shift in voltage for Fe redox. Our combined experimental and computational investigation sheds light on how these complex materials store Li^+ and increase cell voltage. These findings point toward future compositional alterations that may further improve their properties.

Introduction

Electrochemical cation-insertion reactions in solid-state hosts define the function and performance of many advanced rechargeable batteries and related energy-storage devices. Transition-metal oxides and phosphates remain the most common active materials for such purposes, with cation storage accommodated in specific sites within the host structure accompanied by changing oxidation state at metal sites.[1] Metal-site substitution in classic cation-insertion materials provides a path to introduce new storage sites, stabilize the solid-state framework, increase local conductivity, and shift the redox potential.[2] All these factors combine to enhance capacity and increase cycle life, power, and cell voltage in the corresponding batteries.

The transition to more complex multi-metal oxides (e.g., $LiNi_xMn_yCo_{1-x-y}O_2$) and phosphates for Li^+ storage introduces challenges for deconvolving reaction pathways and the roles played by different material components.[3,4] As one example, we previously reported on vanadium-substituted iron oxide (VFe_2Ox) aerogels as a prospective Li^+-storage host, demonstrating that substituting V^{5+} for a fraction of Fe sites in a nominal maghemite (γ-Fe_2O_3) structure significantly increases capacity and shifts the Li^+-insertion toward higher potentials.[5] The capacity and power capability of VFe_2Ox aerogels are further enhanced by adding a third metal cation, electro-inactive Al^{3+}, at lower site concentration.[6] In addition to compositional complexity with multiple metal sites, VFe_2Ox aerogels exhibit structural defects (e.g., cation vacancies) and lack long-range crystallographic order, making characterization by diffraction difficult.

X-ray absorption near-edge spectroscopy (XANES) is often deployed to probe the element-specific oxidation state and local coordination of battery-relevant materials.[7] We use a bench-scale X-ray absorption spectrometer to separately track V and Fe oxidation states *in situ* while the VFe_2Ox electrode is electrochemically conditioned in a lithium pouch cell over its active voltage range (3.8–2.0 V). Parallel computations using exchange-corrected density functional theory (DFT) predict that lithiation of a model VFe_2Ox structure proceeds first with Fe^{3+} reduction at octahedral sites, followed by V^{5+} reduction at tetrahedral sites. The unanticipated shift of $Fe^{2+/3+}$ redox to energetic prominence versus $V^{4+/5+}$, now confirmed by experiment and computation, points to new opportunities to uncover the quantum mechanical-level effects that can be exploited to design optimized charge-storage hosts.

Results and discussion

The epoxide-driven sol–gel process we use to synthesize VFe_2Ox aerogels yields a high surface area, mesoporous material that is amorphous by powder X-ray diffraction.[5] Post-synthesis thermal treatment in flowing air or O_2 removes unwanted

[a] Code 6170, Surface Chemistry Branch, U.S. Naval Research Laboratory, Washington, DC, USA.
[b] Code 6390, Center for Materials Physics and Technology, U.S. Naval Research Laboratory, Washington, DC 20375, USA.

Supplementary Information available: [details of any supplementary information available should be included here]. See DOI: 10.1039/x0xx00000x

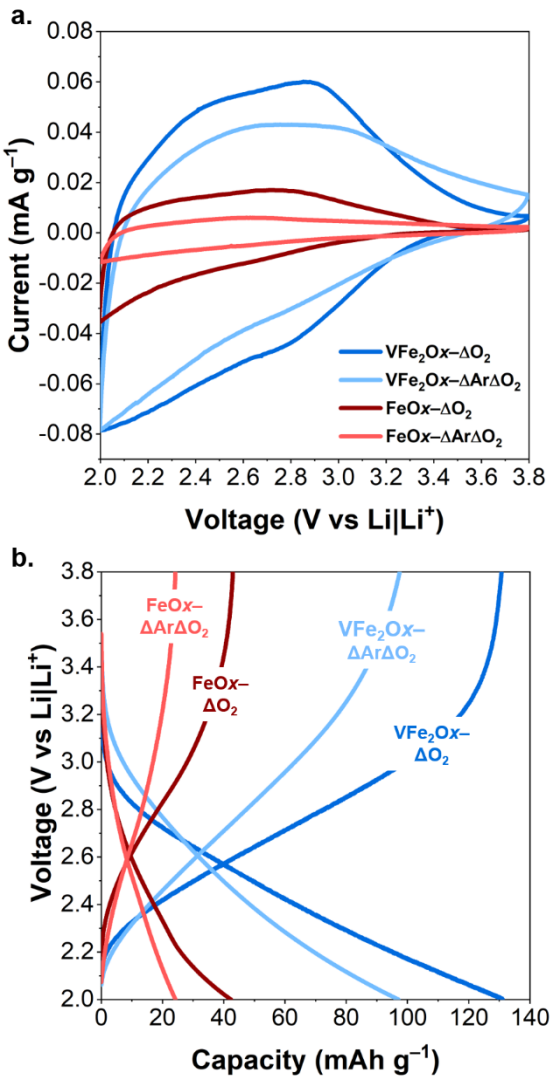

Fig. 1 **a.** Cyclic voltammograms at a sweep rate of 0.1 mV s^{-1} and **b.** galvanostatic charge/discharge at a current density of 100 mA g^{-1} of coin cells comprising aerogel-based VFe_2Ox or FeO*x* cathodes, lithium metal anode, and 1 M LiTFSI in EC/DEC electrolyte.

organic byproducts of the synthesis, but preserves the disordered solid-state structure (Fig. S1) and V^{5+} speciation (product here denoted as oxide heated in specified atmosphere, e.g., $VFe_2Ox–\Delta O_2$). Alternately, heating in low pO_2 (e.g., flowing argon) converts the amorphous VFe_2Ox aerogel to a nanocrystalline spinel form (related to γ-Fe_2O_3), concomitant with partial reduction of V sites to V^{4+}. Subsequent heating under flowing O_2 converts V^{4+} back to V^{5+} while maintaining a nanocrystalline spinel structure (product here noted as $VFe_2Ox–\Delta Ar\Delta O_2$).

We previously showed that metal oxidation state and degree of crystallinity of these VFe_2Ox compositions impact Li^+ insertion capacity.[5] In this report, we use cyclic voltammetric analysis of powder-composite electrodes in 1 M LiTFSI in EC/DEC at slow scan rates (0.1 mV s^{-1}) and find that Li-ion redox in VFe_2Ox spans the 2.0–3.8 V (vs. Li|Li^+) range (Fig. 1a). Iron oxide (FeO*x*) aerogels, prepared by similar methods, but without vanadium substitution, exhibit similar broad features albeit distributed across a narrower voltage window (~2.0–3.1 V vs Li|Li^+) and with substantively lower current density. For both compositions, the disordered O_2-heated materials exhibit higher specific current than their nanocrystalline Ar-O_2-heated analogs, in agreement with our prior reports.[5] Quantitative specific capacity metrics are determined by galvanostatic discharge tests at 100 mA g^{-1} as shown in Fig. 1b. Regardless of the degree of structural order in the aerogel-based active materials, the inclusion of V^{5+} in the FeO*x* composition significantly increases Li-ion capacity; for example capacity increases from 95 mAh g^{-1} for $VFe_2Ox–\Delta Ar\Delta O_2$ to 130 mAh g^{-1} for $VFe_2Ox–\Delta O_2$. In such cases, increased charge-storage capacity may arise from the introduction of additional cation vacancies with V^{5+}-for-Fe^{3+} substitution and/or the participation of both $Fe^{2+/3+}$ and $V^{4+/5+}$ redox.

X-ray absorption spectroscopy provides the opportunity to selectively monitor for Fe and V redox as these VFe_2Ox materials undergo electrochemical Li-ion storage. For such measurements, we first prepare powder-composite electrodes (VFe_2Ox or FeO*x* aerogel, conductive carbon, binder) supported on carbon paper. These cathodes are paired with a lithium metal counter/reference electrode (Cu foil tab maintained outside of the X-ray beam path) and incorporated in a pouch cell configuration (Fig. 2). The resulting pouch cell is mounted in the spectrometer and connected to a potentiostat for

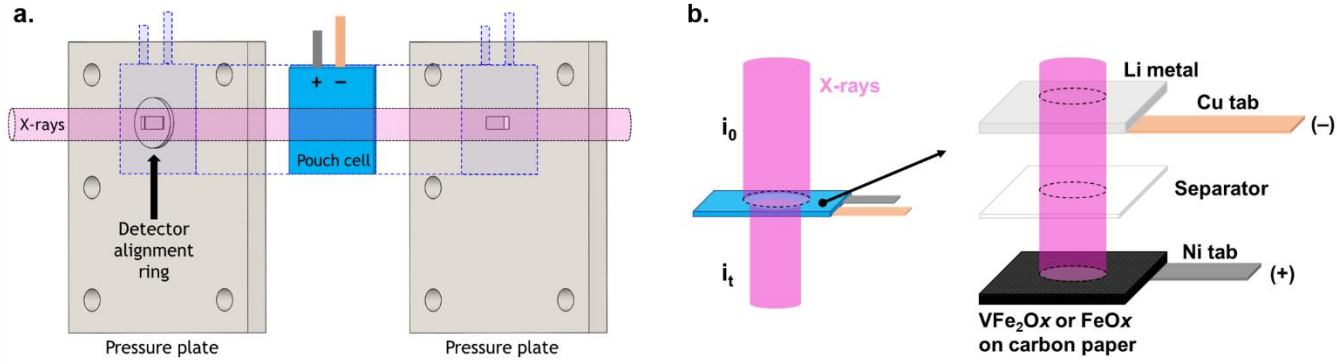

Fig. 2 Schematics of **a.** the cell holder for in situ XANES acquisition and **b.** the pouch cell internal layout with respect to the X-ray beam path (magenta cylinder) for X-ray absorption measurements. The metal tabs used for current collection are positioned outside of the beam path to limit attenuation.

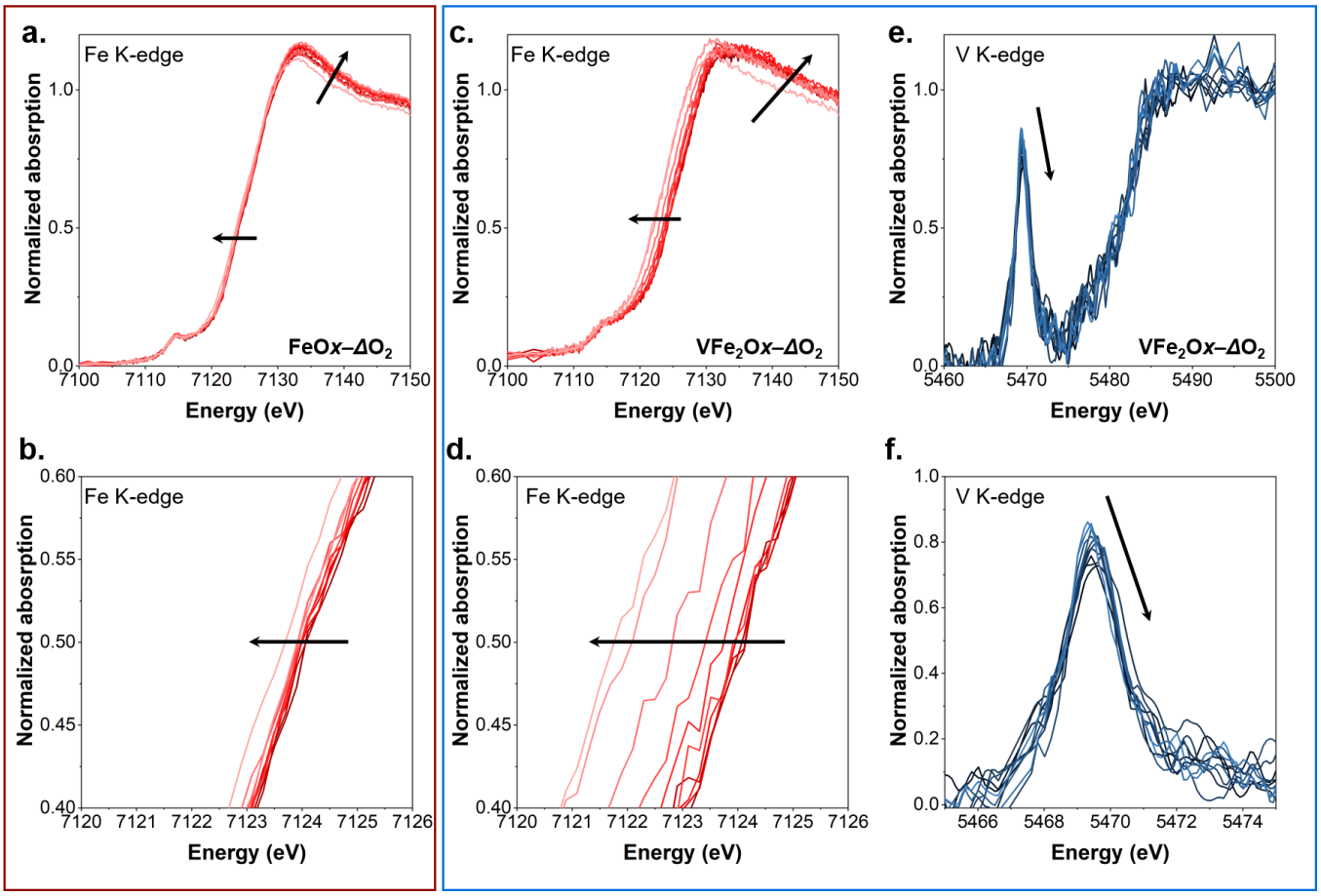

Fig. 3 In situ XANES spectra of pouch cells at the Fe K-edge for **a., b.** FeO*x*–ΔO_2 and **c., d.** VFe_2O*x*–ΔO_2 upon lithiation (discharge). **e., f.** In situ XANES spectra at the V K-edge for VFe_2O*x*–ΔO_2 upon lithiation (discharge). Panels b., d., and f. are inset views of panels a., c., and e., respectively. Arrows denote the direction of lithiation with respect to voltage. See Fig. S2 for corresponding spectra collected during delithiation (charge).

electrochemical control. After three break-in cycles at 1 mV s^{-1}, the pouch cell voltage is stepped in 200 mV increments from 3.8 V down to 2.0 V and X-ray absorption spectra are collected at either the Fe or V K-edge while each voltage step is held.

Iron K-edge X-ray absorption in γ-Fe_2O_3 and related Fe^{3+} iron oxide materials typically consist of a weak pre-edge feature at ~7115 eV followed by a white line that shifts modestly with oxidation-state change.[8] In the present case, lithiation of FeO*x*–ΔO_2 results in a main absorption edge shift of ~1 eV (Fig. 3a,b) in contrast with the nearly 3 eV shift observed in VFe_2O*x*–ΔO_2 (Fig. 3c,d). The larger shifts for the Fe K-edge in VFe_2O*x*–ΔO_2 indicate that a larger fraction of Fe^{3+} sites are reduced to Fe^{2+}, even though VFe_2O*x* has a lower Fe content than FeO*x*. The ability to reduce a higher fraction of Fe^{3+} is a trend consistent with the higher Li^+ storage capacity compared to FeO*x*–ΔO_2.

Vanadium K-edge absorption spectra are generally more complex, often containing a prominent pre-edge peak that arises from distorted V^{5+} octahedra and related coordination (Fig. 3e,f).[9] The pre-edge peak intensity offers a more accurate track of oxidation state as compared to monitoring shifts in the position of the main absorption edge.[10, 11] Upon lithiation of VFe_2O*x*–ΔO_2, we observe a diminution in pre-edge intensity from ~0.85 to ~0.73 and a slight positive shift in peak position, indicative of a fraction of the V^{5+} sites being reduced to V^{4+}.

The nanocrystalline, Ar-O_2-treated analogs to VFe_2O*x*–ΔO_2 and FeO*x*–ΔO_2 aerogels display qualitatively similar trends under electrochemical conditioning, but with less dramatic shifts in Fe K-edge absorption energy (Fig. S3, S4). For example, the VFe_2O*x*–$\Delta Ar\Delta O_2$ material shows only a ~1.5 eV shift in the Fe K-edge compared to ~3 eV for VFe_2O*x*–ΔO_2. The V pre-edge intensity for VFe_2O*x*–$\Delta Ar\Delta O_2$ displays a similar change in overall intensity (~0.12 in normalized absorption), but at a lower initial peak height (0.66 for VFe_2O*x*–$\Delta Ar\Delta O_2$ and 0.86 for VFe_2O*x*–ΔO_2). While the disordered VFe_2O*x*–ΔO_2 is the most practically useful material of this series from a charge-storage perspective, we include the nanocrystalline VFe_2O*x*–$\Delta Ar\Delta O_2$ in our analysis to compare with DFT modeling of vanadium ferrite (see below).

For a quantitative assessment of Fe oxidation state (Fig. 4a), we perform linear-combination analysis on FeO*x* and VFe_2O*x* using γ-Fe_2O_3 (a related defective spinel structure) as a Fe^{3+} standard and FeO (octahedrally coordinated) as a Fe^{2+} standard (Fig. S5a). It is critically important to select standard compounds with similar local coordination (e.g., octahedral Fe vs tetrahedral Fe) for quantitative assessment of oxidation state.[12] Consistent with the low Li^+ storage capacity measured in galvanostatic discharge, FeO*x*–$\Delta Ar\Delta O_2$ aerogel undergoes a

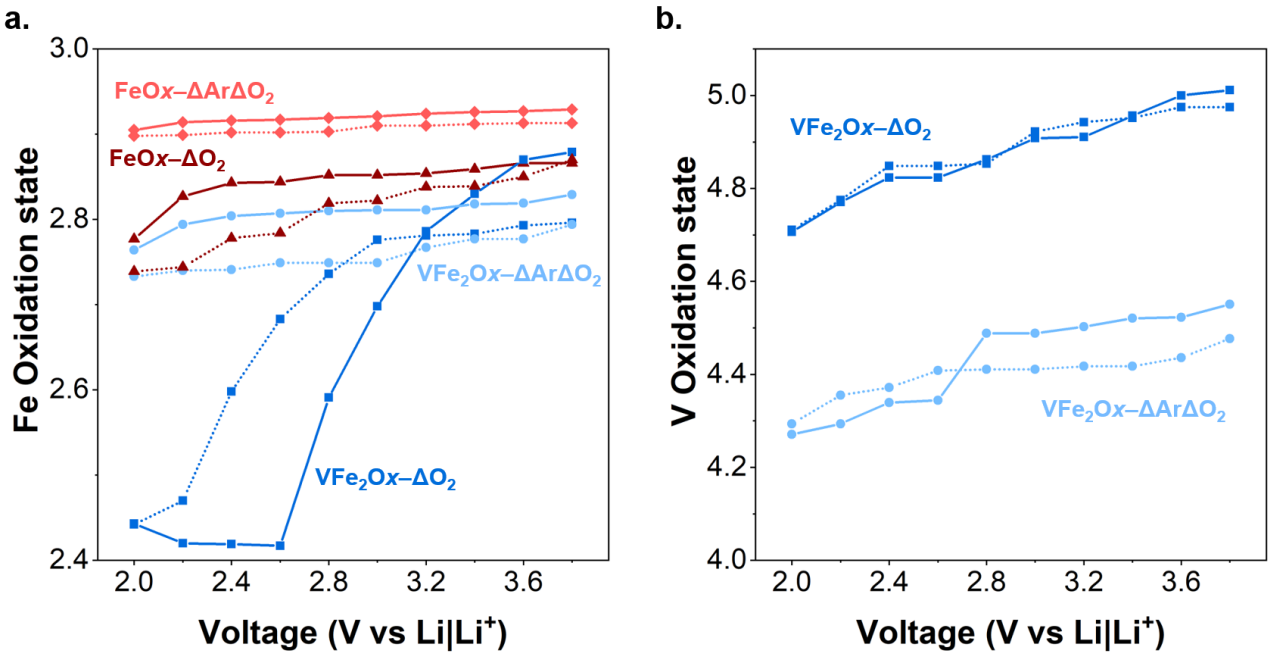

Fig. 4 Oxidation-state tracking from XANES analysis of the K-edges for **a**. iron and **b.** vanadium during electrochemical control between 3.8–2.0 V for lithium pouch cells. Solid lines: lithiation, dotted lines: delithiation.

minimal change in Fe oxidation state (~0.06 e^- per formula unit). The FeO*x*–ΔO_2 aerogel displays a modestly higher oxidation-state change (~0.1 e^-) that occurs primarily in the 2.0–2.7 V range, as typical for maghemite-type Fe_2O_3 when cell voltage is restricted to avoid decomposition to Fe metal and lithium oxide.[13-15]

The XANES-determined 0.1 e^- $Fe^{2+/3+}$ redox change is insufficient to account for the electrochemically measured Li^+ capacity (~43 mAh g^{-1} or 0.26 e^-) for FeO*x*–ΔO_2. Similar divergence between expected Fe oxidation state shift and capacity was observed in a XANES investigation of hollow γ-Fe_2O_3 nanoparticles.[16] The authors ascribed the extra capacity (not accounted for by $Fe^{2+/3+}$ changes) to the participation of proton-stabilized cation vacancies as Li^+ storage sites. Reutschi was the first to discuss proton-stabilized vacancies for charge storage, initially in the case of MnO_2 electrodes operated in aqueous-alkaline electrolyte.[17–19] We extended these concepts from Reutschi's alkaline case to nonaqueous lithium-ion storage[20] to describe enhancements in Li^+-storage capacity for such materials as defective vanadium oxide[21] and Mo-substituted iron oxide.[22]

Average Fe oxidation-state changes for VFe_2Ox–$\Delta Ar\Delta O_2$ aerogel are minimal (2.74–2.83), but energetically dispersed across the operating voltage window (3.8–2.0 V). The most striking example with respect to Fe-based redox is the VFe_2Ox–ΔO_2 aerogel, for which the Fe oxidation state shifts between ~2.8 and 2.45. During discharge, $Fe^{2+/3+}$-supported lithiation commences at ~3.0 V and extends down to 2.0 V, whereas the reverse reaction (delithiation coupled with $Fe^{2+}\rightarrow Fe^{3+}$ redox) begins at ~2.6 V and is complete at ~3.6 V. These results indicate that the presence of V in the FeO*x* structure shifts $Fe^{2+/3+}$ redox to higher average voltage in addition to increasing the number of Fe sites that are redox-active.

We track the V oxidation state as a function of electrochemical conditioning (Fig. 4b) by analyzing the intensity of the V pre-edge peak in reference to V^{4+} and V^{5+} standards in which we select for coordination geometry as well as oxidation state (Fig. S5b).[10, 11] Changes in the vanadium oxidation state for both VFe_2Ox–ΔO_2 and VFe_2Ox–$\Delta Ar\Delta O_2$ occur primarily in the 2.0–2.8 V range, more negative than typically observed for Li^+ storage in vanadium oxides that operate via $V^{4+/5+}$ redox (e.g., V_2O_5)[23]. The cell with a VFe_2Ox–ΔO_2 aerogel cathode has a higher beginning V oxidation state (average $V^{4.9+}$) compared to its VFe_2Ox–$\Delta Ar\Delta O_2$ counterpart (average $V^{4.5+}$), likely due to the initial argon-based heating of the latter. Yet in both cases the overall V oxidation-state change is comparable at ~0.25 e^-.

Because the XANES analyses substantiate that the cell voltage at which Fe redox occurs in these materials is higher than expected for the $Fe^{2+/3+}$ couple in oxides, we focus our attention on the sequence of Fe and V redox. The origin of the increased cell voltage must correspond to a change in the electrochemical potential of the cathode material, so we compare the electronic structure of VFe_2Ox to γ-Fe_2O_3 (maghemite), which has a more typical $Fe^{2+/3+}$ voltage in nonaqueous lithium-based cells. We pay careful attention to the edge of the density of states (DOS) above E_F into which electrons will be deposited during lithiation. We decompose the DOS into its atomic character, known as partial DOS or pDOS. To make our comparison as valid as possible, the vacancy distribution in γ-Fe_2O_3 is the starting point for each of our disordered VFe_2Ox structures, including the lowest energy one, which we adopt for all subsequent calculations (see Experimental).

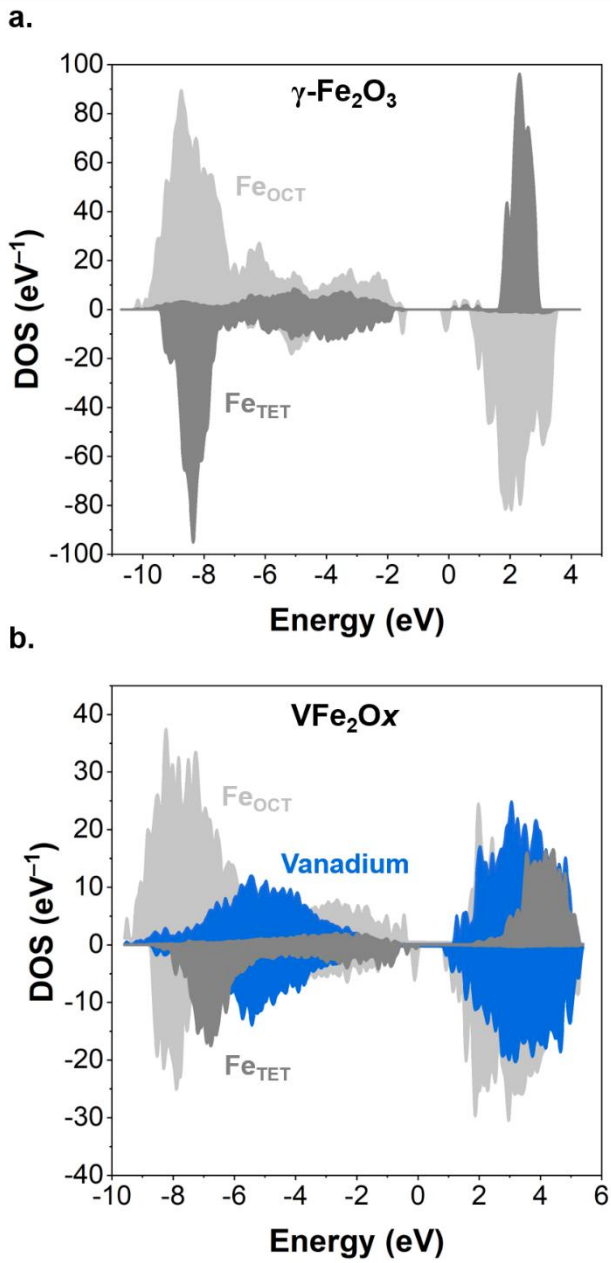

Fig. 5 Partial density of states for **a.** maghemite γ-Fe_2O_3 and **b.** VFe_2Ox. The majority spin ("up") character is plotted along the positive y-axis, while the minority spin ("down") character is plotted on along the negative y-axis.

All Fe atoms converge to a high-spin $\mu=5\mu_B$ (Fe^{3+}) state and all V atoms converge to a non-magnetic (V^{5+}) state for both maghemite and VFe_2Ox (Fig. 5). In the maghemite calculation, the Fe_{tet} and Fe_{oct} moments are uniformly anti-aligned with each other and the overall gap is defined by the exchange splitting. When V is introduced into the structure, its unoccupied states hybridize with Fe, as can be seen by the overlap and matching distribution of peaks of the pDOS (Fig. 5b). For the Fe_{tet} states, hybridization occurs only in the majority spin channel and all Fe_{tet} moments remain fully aligned with each other. In contrast, Fe_{oct} states hybridize with V in both majority and minority spin channels, which flips a significant number of Fe_{oct} moments to now align with Fe_{tet} moments. The importance of this hybridization is that the states now at the top of the gap have strongly hybridized V–Fe_{oct} character, indicating that redox will not be restricted to a single atom type, in agreement with what is actually seen in experiment.

Having established the electronic structure of VFe_2Ox, we proceed to simulate lithiation by adding Li atoms into the structure one by one, relaxing the structure at each concentration, and evaluating the energy. We analyze the newly filled states below E_F in terms of atomic character to establish redox sequence and in terms of energy to establish voltage. In parallel, we add Li to the maghemite structure for comparison. The pDOS for Li_yVFe_2Ox for y=0.06 and y=0.36 respectively represents intercalation scenarios at high voltage (low Li content) and low voltage (high Li content), Fig. 6.

Comparing to the unlithiated DOS, it is clear that as lithiation occurs, electronic states become occupied and move from right to left into the fundamental gap, below E_F. At high voltage, the newly occupied states are predominantly Fe_{oct} with a small minority of V electronic character. At low voltage, the newly occupied states are still predominantly Fe_{oct}, but with a substantially higher proportion of V character. This finding is consistent with our XANES analysis of the redox sequence. In the maghemite structure, it is solely Fe_{oct} that is reduced (not shown), which is consistent with crystallographic investigations of lithiation of this oxide.[14] This preference to initiate reduction of Fe sites over V sites in VFe_2Ox upon lithiation reflects the importance of hybridization between V and Fe.

We calculate the average voltage of lithiated VFe_2Ox according to the procedure of Aydinol and Ceder,[24] which can be distilled to Equation 1:

$$V_{ave} = \frac{E[Li_{y_1}VFe_2O_x] - E[Li_{y_2}VFe_2O_x] - (y_2 - y_1) * E[Li]}{(y_2 - y_1)} \quad \textbf{Equation 1}$$

Where $E[]$ is the total energy in eV of the compound in brackets as calculated by DFT. If multiple calculations at multiple values of y_1 and y_2 are available, a step-wise calculation of the voltage profile can be made. This type of calculation is useful for multiple-phase materials in which one or more plateaus occur. However, because of extensive disorder in our aerogel-based materials, we occasionally find very low or very high energy sites for Li^+ within our structure. This variance causes the step-by-step profile to be too jumpy to convey reasonable information. Experimentally, the lack of plateaus in the charging curves (Fig. 1) indicates that VFe_2Ox is a solid solution material with respect to Li intercalation, so E should depend linearly on y with a slope equal to the average voltage:

$$V_{ave} = \frac{\Delta E}{\Delta y} - E[Li] \quad \textbf{Equation 2}$$

we fit our data points to a line and calculate the slope, which gives us an overall average between the endpoints. The best line fit to the energies of maghemite Fe_2O_3 and VFe_2Ox at various Li^+ concentrations are 2.46 V for maghemite and 3.35 V for VFe_2Ox, as referenced to Li|Li^+ (Fig. S6). This voltage increase for VFe_2Ox demonstrates that hybridization of V with Fe is

responsible for the dual cationic redox seen in VFe_2Ox and also explains the unexpected redox voltage seen in XANES and validated here with DFT. This hybridization between V and Fe (as well as the standard hybridization with oxygen) effectively shifts the energy of the conduction band maximum of VFe2Ox downward compared to maghemite, raising the electronic chemical potential of the former. Practically, this hybridization results in an increased potential vs $Li|Li^+$, making VFe_2Ox a more desirable material for positive electrodes in lithium-based batteries

As described in the Experimental section, we calculate the ground state of multiple VFe_2Ox structures with various levels of disorder. In one of these (not the lowest energy one), two of the random oxygen vacancies are located adjacent to a V atom. In this case, the under-coordinated V atom converges to V^{4+} (μ=1 μ_B); see Fig. S7 for the pDOS of this calculation. The basic structure of the pDOS of Fe_{oct}, Fe_{tet}, and V remains similar to other DFT calculations but the pDOS of the single V^{4+} shows a sharp peak below the y-axis around –2 eV without a compensating peak on the positive y-axis. The presence of this spin-polarized occupied state only in the presence of concentrated oxygen vacancies indicates that these defects are the cause of V^{4+} in unlithiated VFe_2Ox. This finding is entirely consistent with the difference in XANES spectra as a function of heat treatment, with the O_2 treatment filling oxygen vacancies and thus suppressing V^{4+}.

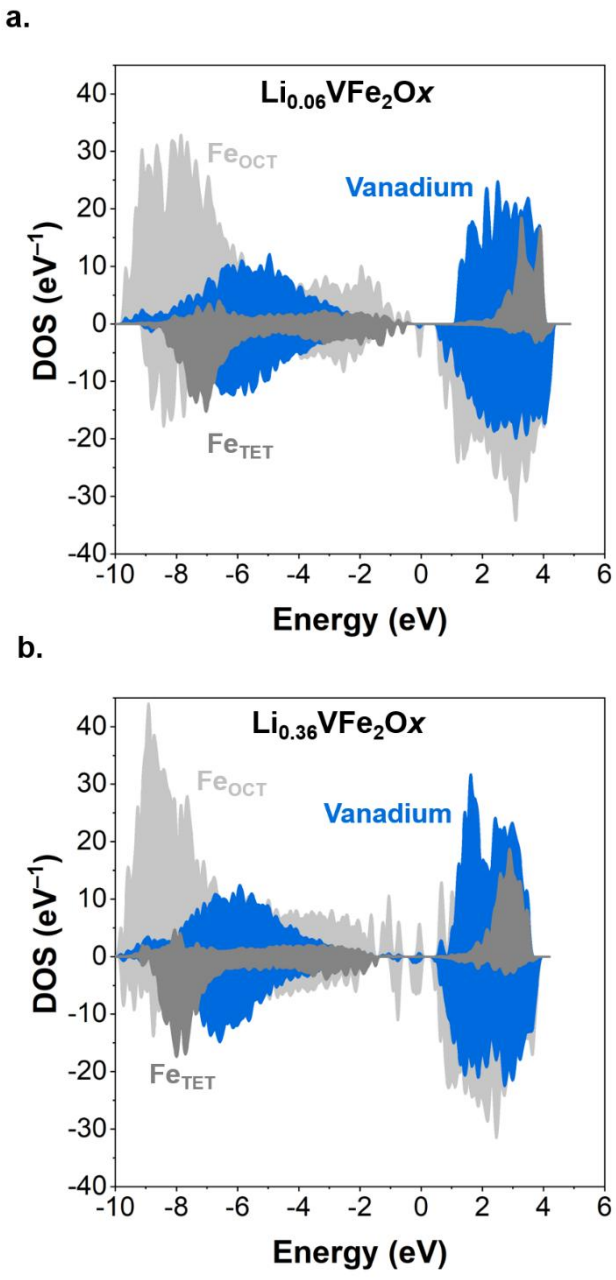

Fig. 6 Partial density of states for VFe_2Ox at **a.** 0.06 Li^+ per formula unit (low Li content) and **b.** 0.36 Li^+ per formula unit (high Li content).

In a gapped material, first-order perturbation theory gives the hybridization strength as t^2/U, where t is the orbital overlap and U is the energy distance between atomic-like orbitals prior to mixing in the material (derivation in Supplemental Information). The strength of the hybridization, and therefore the energy height of the empty (anti-bonding) states that determine voltage, can be increased in one of two ways: (*1*) increasing the overlap or (*2*) decreasing the energy nearness of the hybridizing species. Moving downward in the periodic table accomplishes the first. For example, substituting Nb or Ta in place of V might preserve all other relevant aspects, namely the oxidation state of the substituent, while increasing the extent of the d-orbitals by moving from 3d to 4d to 5d. Another option is to move rightward along the periodic table towards Fe in order to shrink the energy denominator. Cr or Mn are suitable in this regard, but the change in oxidation state (neither will assume the 5+ state that exists in V) complicates the analysis. Previous work shows that substitution of Mo,[22] which is a shift both to the right and down on the periodic table, indeed raises the cell voltage, providing confirmation of a fruitful strategy to further improve the performance of disordered ferrite materials.

Conclusions

Disordered vanadium ferrite VFe_2Ox exhibits lithium charge storage at both iron and vanadium sites. Our XANES analyses establish that vanadium substitution shifts iron redox to more positive, technologically valuable voltages as compared to unsubstituted maghemite. In corroboration of these experiments, density functional theory reveals that hybridization of V and Fe orbitals imparts concomitant redox of both elements. Our findings lay the framework for intentional synthetic substitution into FeO*x* that may further improve electrochemical energy storage.

Experimental Section

Material synthesis

VFe_2Ox and FeO*x* aerogels were synthesized using a modification of the method described previously.[5] Briefly, ~ 100 mL of ethanol were chilled in an ethanol/dry ice bath. 6.16 g (22.8 mmol) of $FeCl_3 \cdot 6H_2O$ were dissolved in 20 mL of

chilled ethanol in a glass beaker. Separately, 2.76 g (11.3 mmol) of vanadium (V) oxytriisopropoxide (VTIP) was dissolved in 40 mL of chilled ethanol while stirring, producing a cloudy white/yellow solution. The $FeCl_3 \cdot 6H_2O$ solution was quantitatively transferred to the VTIP solution, producing a clear orange solution. To this solution, 24 mL of propylene oxide (passed through a column of activated alumina) was added quickly, while stirring. This solution was covered with parafilm and stirred while chilling in a water-ice bath. After 30 min, the solution was allowed to warm to room temperature naturally and without stirring, during which time the solution turned a dark brown color. After 1 h at room temperature, the solution became a dark brown gel. The gel was aged for 24 h covered and unstirred. After aging, the gel was fragmented into small chunks with a spatula and washed three times with ethanol and dried using vacuum filtration. The rinsed gel was resuspended in ethanol (solution replaced twice daily for two days) after which time it was resuspended in acetone (solution replaced twice daily for two days). After the final acetone suspension, the majority of the acetone was poured off and the gel was loaded into a Leica EM CPD300 auto-dryer sample cup and dried in supercritical CO_2. FeO*x* aerogels were prepared similarly, but without the addition of VTIP.

After solvent exchange with supercritical CO_2, the as-dried VFe_2Ox or FeO*x* aerogels were ground to a very fine powder using a spatula. The molar ratio of metals in VFe_2Ox aerogels was confirmed (~2.8:1 Fe:V) using a SciAps X-200 X-ray fluorescence analyzer. To prepare the O_2 heat-treated samples ($VFe_2Ox–\Delta O_2$ or FeO*x*–ΔO_2), the powder was loaded into an alumina boat and placed in a tube furnace. Under flowing O_2, the reactor was heated to 325 °C with a 5 h ramp, held at 325 °C for 4 h, then cooled over 5 h to 25 °C. $VFe_2Ox–\Delta Ar\Delta O_2$ and FeO*x*–$\Delta Ar\Delta O_2$ samples were prepared under the same thermal conditions, but by first treating under flowing argon, followed by the same thermal treatment under flowing O_2. The nitrogen physisorption surface area and pore volume of FeO*x*–$\Delta Ar\Delta O_2$ were measured on a Micromeritics ASAP 2020 porosimeter. These values are compared to prior published results[5] for $VFe_2Ox–\Delta O_2$, $VFe_2Ox–\Delta Ar\Delta O_2$, and FeO*x*–$\Delta O_2$ in Table S1.

Preparation of electrodes

Active material (VFe_2Ox or FeO*x*) and conductive carbon Super P (Alfa Aesar) were separately ground with a mortar and pestle for 5 min each. For a typical flag electrode, a 1.5 cm × 2.5 cm piece of carbon paper (60 gsm buckypaper, NanoTechLabs) was cut and adhered to a 1 cm × 5 cm carbon-coated aluminum current collector using carbon paste (Ted Pella, DAG-T-502). For the electrode slurry, 20 mg active material and 2.5 mg Super P were combined and mixed well, to which 150 µL of 20 mg mL^{-1} polyvinylidene fluoride (PVDF, Kynar) in N-methyl pyrrolidone (NMP, Aldrich) was added. The resultant mixture was stirred until homogeneous, drop-casted onto the carbon paper portion of the flag electrode, and smoothed with a razor blade over an area of 1.5 cm × 1.5 cm. The NMP was removed by placing the electrode in a 50°C oven overnight.

Preparation of pouch cells for X-ray absorption spectroscopy

For typical pouch-cell preparation, a lithium chip (MTI corp.) was flattened between polypropylene sheets in an argon-filled glovebox until the area matched that of the carbon paper flag electrode. The lithium metal rectangle was then attached to a 1 cm × 5 cm copper current collector. The cathode, anode, and Celgard separator (Type 2500) were assembled within an aluminum-lined pouch-cell casing (MFC), which was then heat-sealed on three sides. To the pouch, 300 µL of electrolyte were added [1 M LiTFSI (Sigma-Aldrich, 99.95%) in EC/DEC (Aldrich, Sigma-Aldrich, 1:1 vol)]. The EC/DEC solvent was stored on activated 3 Å molecular sieves for at least a week before mixing with the LiTFSI salt. The pouch was vacuum sealed on the final side and then used in electrochemical/XAS experiments.

X-ray absorption measurements

Iron and vanadium K-edge XANES (X-ray absorption near-edge spectroscopy) spectra were collected (easyXAFS 300+) on the pouch cells described above on subsequent cycles (Fe K-edge followed by V K-edge). Prior to XANES measurements, cells were preconditioned voltammetrically (Gamry Ref 620) at 1 mV s^{-1} from 2.0–3.8 V for three cycles. For in situ XANES measurements[25], the cell voltage was swept at 1 mV s^{-1} between voltage points of interest and held potentiostatically during XANES acquisition. At each point of interest, the voltage was held for 30 min to allow the cell to reach a steady-state current before XANES spectra were collected. XANES spectra were collected first at the iron K-edge followed by the vanadium K-edge after switching the spherically bent crystal analyzer from Si (531) to Ge (211). Metallic iron and vanadium foils were used to calibrate the energy at 7112 and 5465 eV for the Fe K-edge and the V K-edge, respectively. Three consecutive spectra (~30 min per scan) were collected and averaged for each voltage of interest. Linear combination analysis (LCA) was used to assess the oxidation state of Fe and V in VFe_2Ox and FeO*x* using the following standard compounds: γ-Fe_2O_3 (Fe^{3+}, O_h and T_d coordination), FeO (Fe^{2+}, O_h coordination), Na_3VO_4 (V^{5+}, T_d coordination), and $VOSO_4 \cdot xH_2O$ (V^{4+}, distorted O_h coordination). Fitting of the main absorption edge and the pre-edge was used for the iron K-edge and vanadium K-edge, respectively.

Computational methods

All density functional theory (DFT) calculations were done using the Vienna Ab-initio Simulation Program (VASP)[26] with the projector augmented wave (PAW) method.[27] A supercell containing 147 atoms was created with the stoichiometry $V_{17}Fe_{35}O_{95}$ which allowed for a formal valence of 5^+, 3^+, and 2^- for all V, Fe, and O atoms respectively. V atoms were placed exclusively, but randomly, at tetrahedral sites and Fe atoms at both tetrahedral and octahedral sites with compensating cation vacancies distributed randomly on octahedral sites. Tests to determine that random tetrahedral V and octahedral vacancy site distribution produced the lowest energy structure were conducted against the following scenarios: ordered octahedral distribution, clustered octahedral distribution, random tetrahedral/octahedral distribution, clustered V distribution

and ordered V distribution. Each structure was fully relaxed, both lattice and atomic positions, with the Perdew–Burke–Ernzerhof (PBE)[28] exchange correlation potential with an energy cutoff of 670 eV. Spot tests intended to verify that the PBE-relaxed structures would not substantially change with an HSE-relaxation were performed and both volume and atomic positions changed by <1% with no visible differences in electronic structure. Subsequently, the lattice and positions were frozen and a one-time evaluation with the Heyd–Scuseria–Ernzerhof (HSE)[29] exchange correlation potential with a cutoff of 400 eV was performed for an accurate energy and electronic structure calculation that better accommodates the localized states of Fe and V. HSE calculations employed 0.25 of the short-range exact Hartree–Fock exchange, and the screening parameter, μ, was empirically set to 0.2 (1/Å). All vanadium ferrite calculations were done with gamma-point only; a test calculation with a 2×2×1 k-mesh produced no detectable changes in the density of states. Prior to relaxation, we initially established fully aligned magnetic moments on Fe_{oct} and Fe_{tet} in maghemite, but these relaxed to a converged, lowest energy configuration in which all Fe_{oct} moments are anti-aligned with all Fe_{tet} moments,[26] indicating a strong antiferromagnetic exchange coupling. Therefore, subsequent calculations of maghemite with Li added and of vanadium ferrite with and without Li added all started from the anti-aligned configuration. Lithium atoms were originally placed randomly in areas where they were able to fit without unreasonably small distances between them and other atoms. After the system (lattice and ions) was relaxed, the structure in Fig. S8 was achieved. Relaxation and self-consistency often disrupted this pattern to varying degrees as a function of Li added.

Author contributions

We strongly encourage authors to include author contributions and recommend using CRediT for standardised contribution descriptions. Please refer to our general author guidelines for more information about authorship.

Conflicts of interest

D.R.R. and J.W.L. are inventors on patents (issued to the U.S. Navy) that are related to increasing Li-ion capacity of battery active materials by deliberately forming cation-vacant metal oxides: US Patents no 7,618,609, 8,388,867, 8,790,612, and 9,466,831.

Data availability

The data supporting this article have been included as part of the Supplementary Information.

Acknowledgements

This work was supported by the Office of Naval Research (N0001423WX00604). H.O.F. was an NRL–National Research Council Postdoctoral Associate (2021–2024).

References

1 A. Manthiram, *Nat. Commun.*, 2020, **11**, 1550.
2 A. Hebert and E. McCalla, *Mater. Adv.*, 2021, **2**, 3474–3518.
3 Z. Cui, Z. Guo and A. Manthiram, *Adv. Energy Mater.*, 2023, **13**.
4 M. Yi, W. Li and A. Manthiram, *Chem. Mater.*, 2022, **34**, 629-642.
5 C. N. Chervin, J. S. Ko, B. W. Miller, L. Dudek, A. N. Mansour, M. D. Donakowski, T. Brintlinger, P. Gogotsi, S. Chattopadhyay, T. Shibata, J. F. Parker, B. P. Hahn, D. R. Rolison and J. W. Long, *J. Mater. Chem. A*, 2015, **3**, 12059-12068.
6 C. N. Chervin, R. H. DeBlock, J. F. Parker, B. M. Hudak, N. L. Skeele, J. S. Ko, D. R. Rolison and J. W. Long, *RSC Adv.*, 2021, **11**, 14495-14503.
7 F. Lin, Y. Liu, X. Yu, L. Cheng, A. Singer, O. G. Shpyrko, H. L. Xin, N. Tamura, C. Tian, T.-C. Weng, X.-Q. Yang, Y. S. Meng, D. Nordlund, W. Yang and M. M. Doeff, *Chem. Rev.*, 2017, **117**, 13123-13186.
8 A. Boubnov, H. Lichtenberg, S. Mangold and J. D. Grunwaldt, *J. Synchrotron Rad.*, 2015, **22**, 410-426.
9 F. Benzi, G. Giuli, S. Della Longa and E. Paris, *J. Synchrotron Rad.*, 2016, **23**, 947-952.
10 P. Chaurand, J. Rose, V. Briois, M. Salome, O. Proux, V. Nassif, L. Olivi, J. Susini, J.-L. Hazemann and J.-Y. Bottero, *The Journal of Physical Chemistry B*, 2007, **111**, 5101-5110.
11 A. Levina, A. I. McLeod and P. A. Lay, *Chem. Eur. J.*, 2014, **20**, 12056-12060.
12 J. Zhu, Z. Zeng and W.-X. Li, *J. Phys. Chem. C*, 2021, **125**, 26229-26239.
13 C. N. Lininger, C. A. Cama, K. J. Takeuchi, A. C. Marschilok, E. S. Takeuchi, A. C. West and M. S. Hybertsen, *Chem. Mater.*, 2018, **30**, 7922-7937.
14 M. M. Thackeray, W. I. F. David and J. B. Goodenough, *Mater. Res. Bull*, 1982, **17**, 785–793.
15 J. Manuel, J.-K. Kim, J.-H. Ahn, G. Cheruvally, G. S. Chauhan, J.-W. Choi and K.-W. Kim, *J. Power Sources*, 2008, **184**, 527-531.
16 B. Koo, H. Xiong, M. D. Slater, V. B. Prakapenka, M. Balasubramanian, P. Podsiadlo, C. S. Johnson, T. Rajh and E. V. Shevchenko, *Nano Lett.*, 2012, **12**, 2429-2435.
17 P. Ruetschi and R. Giovanoli, *J. Electrochem. Soc.*, 2019, **135**, 2663-2669.
18 P. Ruetschi, *J. Electrochem. Soc.*, 2019, **131**, 2737-2744.
19 P. Ruetschi, *J. Electrochem. Soc.*, 2019, **135**, 2657-2663.
20 B. P. Hahn, J. W. Long and D. R. Rolison, *Acc. Chem. Res.*, 2013, **46**, 1181-1191.
21 K. Swider-Lyons, *Solid State Ionics*, 2002, **152-153**, 99-104.
22 B. P. Hahn, J. W. Long, A. N. Mansour, K. A. Pettigrew, M. S. Osofsky and D. R. Rolison, *Energy Environ. Sci.*, 2011, **4**.
23 R. Baddour, J. P. Pereira-Ramos, R. Messina and J. Perichon, *J. Electroanal. Chem.*, 1991, **314**, 81-101.
24 M. K. Aydinol and G. Ceder, *J. Electrochem. Soc.*, 1997, **144**, 3832-3835.
25 R. H. DeBlock, M. J. Lefler, Z. G. Neale, C. T. Love, J. W. Long and R. Carter, *Energy Adv.*, 2024, **3**, 424–429.
26 G. Kresse and J. Furthmüller, *Phys. Rev. B*, 1996, **54**, 11169-11186.
27 P. E. Blochl, *Phys. Rev. B*, 1994, **50**, 17953-17979.
28 J. P. Perdew, K. Burke and M. Ernzerhof, *Phys. Rev. Lett.*, 1996, **77**, 3865-3868.

29 J. Heyd, G. E. Scuseria and M. Ernzerhof, *J. Chem. Phys.*, 2003, **118**, 8207-8215.

Deconvolving lithium-ion redox in vanadium-iron oxide aerogels using X-ray absorption spectroscopy and density functional theory

Data availability statement

The data supporting this article have been included as part of the Supplementary Information.